



TECHNICAL ARTICLE

Effects of Heat Treatment on Microstructure and Wear Behavior of Modified Aluminum Bronze Coatings Fabricated by Laser Cladding

T.Y. Yin, S. Zhang, F.Q. Zhou, R.J. Huo, C.H. Zhang, and J. Chen

Submitted: 25 June 2021 / Revised: 19 November 2021 / Accepted: 2 December 2021 / Published online: 6 January 2022

In this paper, the effects of heat treatment on microstructure and properties of modified aluminum bronze alloy coatings were studied. In order to clear out this question, Cu-7Al-3Fe-3Ni alloy was fabricated on 316 stainless steel by laser cladding. And a subsequent heat treatment which tempered four samples at 500, 600, 700 and 800 °C for 1 h, respectively. The deposited coatings mainly contained α -Cu, β' (AlCu₃), κ ((Fe,Ni)Al) and Cr-Fe phases according to the analysis of XRD and SEM images. After tempered at 500 °C for 1 h, content of κ phase in the coating increased, and there was residual β' phase. These two hard phases made the coating tempered at 500 °C had the lowest coefficient of friction and wear rate. Then with the increase of tempering temperature, both α -Cu and other phases became coarsen. The results of microhardness showed that the microhardness was significantly improved after heat treatment. Especially, the samples which tempered at 500 °C for 1h showed a better performance of microhardness. With the tempered temperatures increased, the microhardness at interface decreased from 517 HV (500 °C) to 312 HV (800 °C). The EBSD results showed that there was no obvious preferred orientation for grains of deposited and tempered samples, and the Schmidt factor and KAM were both significantly decreased after heat treatment.

Keywords laser cladding, microhardness, microstructure evolution, modified aluminum bronze coating, wear behavior

1. Introduction

Due to the combination of strength, corrosion resistance and wear resistance, aluminum bronze is one kind ideal material for surface modification (Ref 1-3). At present, aluminum bronze block with a good relative density and formability could be prepared by casting, plasma transferred arc (PTA) (Ref 4), wire-arc additive manufacturing (WAAM) (Ref 5) and many other methods (Ref 6). But for the preparation of aluminum bronze coatings, the method was very limited. However, in these existed preparation methods of aluminum bronze coatings, there were still many problems during the process of coatings preparation and the results of the coatings preparation were not lived up to expectation. Such as sputtering occurred in the deposited process of plasma spraying (Ref 7), resulting in the decrease of the density of the aluminum bronze. And the composition of aluminum bronze coatings prepared by physical vapor deposition (PVD) and ion plating was uneven (Ref 8, 9).

Among various surface modification technologies, laser technology has a unique position. Laser surface modification could produce layers or treatment areas with microstructures and compositions that cannot be obtained by other techniques, as well as many other desired properties (Ref 10, 11). However, there were few reports on laser cladding aluminum bronze coatings.

In order to perfect the properties of aluminum bronze, adding alloy elements to aluminum bronze was usually carried out. When a certain amount of Fe and Ni added to pure aluminum bronze, there would be an additional κ phase which presented a high microhardness and small grain sizes that could improve the microstructure and properties of aluminum bronze (Ref 12). Sandeep et al. (Ref 13) changed the Ni content of the surface of the aluminum bronze to improve the microhardness and wear resistance of aluminum bronze. Tao et al. (Ref 14) studied the microstructure and properties of aluminum bronze with different contents of Fe and Ni. In addition to the addition of alloy elements, the microstructure and properties of aluminum bronze could also be optimized by heat treatment (Ref 15, 16). It was reported that high pressure heat treatment had a great contribution to the refinement of grains and could increase the microhardness (Ref 17). And the effect of heat treatment on wear resistance and tensile properties has also been reported (Ref 18). There were few reports on the effects of heat treatment on aluminum bronze fabricated by laser cladding. And it could be predicted that the heat treating temperatures and holding time should be different from cast/wrought aluminum bronze. Timothy et al. (Ref 19) reported that aluminum bronze bulks by selective laser melting (SLM) achieved a higher yield limit and tensile strength than cast/wrought samples after heat treatment at 600-700 °C for 1 h. In

T.Y. Yin, S. Zhang, F.Q. Zhou, R.J. Huo, and C.H. Zhang, School of Materials Science and Engineering, Shenyang University of Technology, Shenyang 110870 Liaoning, People's Republic of China; and J. Chen, Shenyang Dalu Laser Technology CO., LTD, Shenyang 110136 Liaoning, People's Republic of China. Contact e-mails: songzhang_sy@163.com and zhangch5858@126.com.

addition to the two standard heat treatments for cast aluminum bronze, Dharmendra et al. (Ref 20) selected an additional heat treatment temperature which was 550 °C for aluminum bronze prepared by wire-arc additive manufacture. The maximum tensile strength of the sample was obtained after holding at 550 °C for 4 h. This study adopted a heat treatment method of tempering samples at 500, 600, 700 800 °C for 1 h, respectively. The above heat treatment was all for aluminum bronze block, but for the coatings, the heat treatment results of aluminum bronze coatings would be affected by the diffusion of substrate elements. Therefore the changes of microstructures and properties of modified aluminum bronze coatings after heat treatment still need to be studied.

Therefore, a modified aluminum bronze coating would be fabricated on 316 stainless steel surface by laser cladding in this study. And the aluminum bronze coatings would be tempered at four different temperatures, respectively. The microstructure evolution of as deposited and tempered aluminum bronze coatings were studied by x-ray diffraction (XRD), scanning electron microscopy (SEM) and electron back-scatter diffraction (EBSD), aiming to clarify the relationship between microstructure and tempered temperatures as well as the impact of tempered temperatures on the properties of aluminum bronze coatings. This paper would provide a theoretical basis for the heat treatment process of laser cladding modified aluminum bronze coatings.

2. Experiment

2.1 Materials and Methods

The direct used alloy powder was supplied by BGRIMM Advanced Materials Science and Technology Co., Ltd. Aluminum bronze powder was produced by vacuum atomization technology within a particle size range of 45-140 μm. The chemical composition of alloy powder is shown in Table 1. Before the laser cladding process, the alloy powder was dried in a YZG-5 vacuum desiccator at 120 °C for 12 h. The material used in this experiment as a substrate was 316 austenitic stainless steel sheet (100 mm × 100 mm × 10 mm). The chemical composition of 316 stainless steel is in wt.%: ≤ 0.08% C, ≤ 1% Si, ≤ 2% Mn, ≤ 0.035% P, ≤ 0.03% S, 10-14% Ni, 16-18.5% Cr, 2-3% Mo, and Fe balance. The stainless steel substrate needed to be ground with 600 grit SiC paper to clean the surface to remove the oxides or contaminants and then sandblasted to increase surface roughness to enhance powder adhesion.

In this work, a semiconductor laser beam (Laserline, LDF 6000-60) with a 3 mm spot diameter, 980 nm wavelength, laser power of 2500 W and scanning speed of 1500 mm/min was employed to fabricate the aluminum bronze. Figure 1 is the schematic diagram of the laser cladding system and prepared samples. The whole process was carried out under the protection of argon flow with a flow rate of 15 L/min and the powder feeding rate is 20 g/min.

Four groups of deposited samples were tempered at different temperatures (500, 600, 700, 800 °C) for 1 h, respectively, to investigate the effects of heat treatment on the deposited coatings. Box type electric furnace (KSS-1600) was carried out to temper the samples. After the furnace temperatures raised to 500, 600, 700, 800 °C respectively, the samples loaded in the crucible were sent into the furnace, and started timing when the furnace temperature reached the specified temperatures. After holding for 1 h, removed the samples from the furnace and cooled to room temperature in air.

2.2 Microstructural Characterization

The phase identification was studied via x-ray diffraction (XRD, XRD-7000) with Cu Kα radiation at 40 kV and 30 mA. Scanning 2θ range was from 20°-100° at a scanning speed of 4°/min. The microstructure of the samples were observed using scanning electron microscopy (SEM, Hitachi S-3400) equipped with energy dispersive spectroscopy (EDS). The samples were grounded with 60# to 2000# abrasive paper and then polished using a 2.5 μm polishing paste, finally etched in the corrosion solution (5 g FeCl₃ + 50 ml HCl + 100 ml H₂O) for 8 s. Gemini SEM 300 equipped with an electron backscattered diffraction (EBSD) was performed on both deposited and heat treated samples to analysis the grain size, grain orientation and texture. The EBSD samples were firstly grounded with sandpaper (60# - 2000#) and polished with 2.5 and 1.5 μm polishing paste, then mechanical polished for 2 h using the chemical polishing solution. The cross section of the samples were scanned at 2000 × magnification with a step of 0.3 μm.

2.3 Microhardness and Wear Test

HVS-1000 Vickers hardness tester was employed to measure the microhardness of the cross section of aluminum bronze layer. The test load was set to 3 N and the dwelling time was set to 15 s. The interval between each indent was 100 μm in order to ensure the accuracy of the data, the final result was calculated as the average value of 3 points at the same depth range.

A reciprocating wear tester (Lanzhou Institute of Chemical Physics, MFT-4000) was used to test friction and wear properties of coatings, and the tested surface needed to be polished before wear test. The load carried in dry sliding wear test was 10 N and testing time was 30 min. The friction pair was a corundum ball with a diameter of 7 mm. Sliding speed was 100 mm/min and scratch length was 7 mm. Friction coefficient of the coatings was recorded in time during wear test and wear volume was measured with white light interferometer (KLA-Tencor Corporation, Micro XAM-3D). Wear rate (u) was calculated by formula (1):

$$u = \frac{V}{F \cdot L} \quad (\text{Eq 1})$$

where V represents wear volume, F corresponds applied load and L represents the sliding distance (Ref 21).

Table 1 Nominal composition of Cu-7Al-3Fe-3Ni alloy powder (wt. %)

	B	C	Cr	Si	Mo	Mn	Ni	Al	Fe	Cu
Cu-7Al-3Fe-3Ni	0.09	0.01	0.66	0.13	0.04	0.02	3.08	6.72	3.17	Bal.

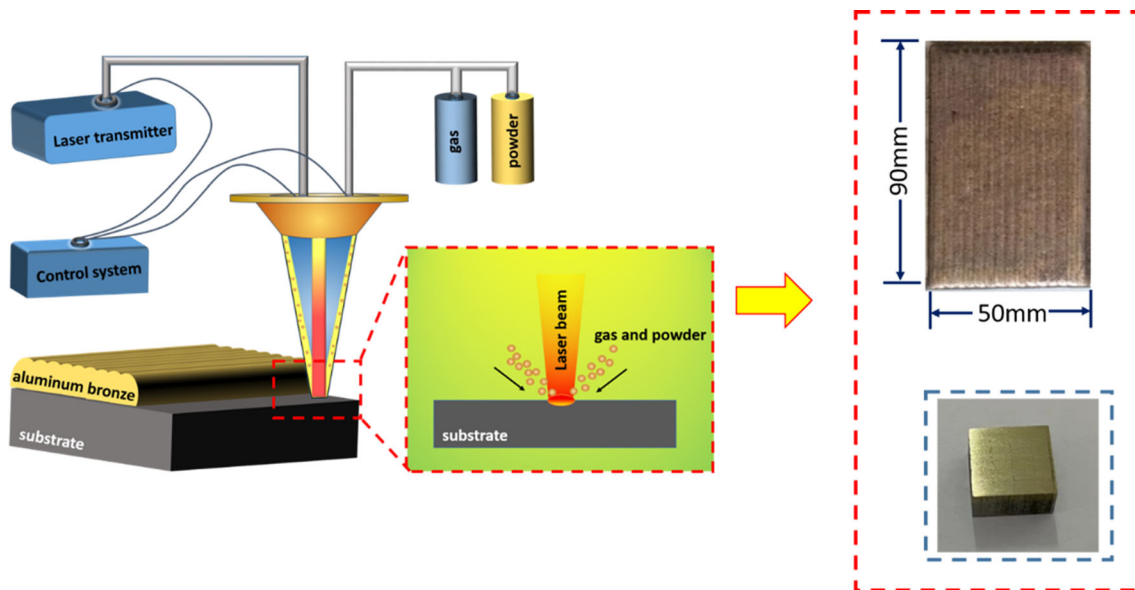


Fig. 1 Laser cladding process schematic diagram of aluminum bronze on 316 stainless steel

3. Result

3.1 Microstructural Evolution

The phase composition of aluminum bronze coatings tempered under five states are shown in Fig. 2. Phases types existed in the deposited and tempered coatings were identical. Diffraction peaks of α -Cu (FCC), β' phase (AlCu₃) and κ (Fe, Ni)Al could be detected on the coating surface. Unconventional Fe-Cr phase occurred in aluminum bronze coatings tempered samples. Beside the difference of phase types in different coatings, the phase content changed obviously under different tempering temperatures.

The aluminum bronze powder was completely transformed into β phase during melting process, and a series complex solid-state phase transitions took place subsequently. Under a high cooling rate, the available non-equilibrium solidification conditions inhibit the eutectoid reaction of β phase ($\beta \rightarrow \alpha + \kappa$) (Ref 22). Therefore, there was β' generated through non-equilibrium solidification in deposited coating. Since the four tempering temperatures were all below the eutectoid reaction, the eutectoid reaction of β phase was fully carried out during the tempering process. The result was the content of α and κ in tempered samples increased significantly than that in deposited status, but the content of β' decreased.

The reason for the formation of Fe-Cr phase was that the solubility of Fe at room temperature was so poor, only about 0.3%. Beyond the scope of that the precipitation of κ phase would occur. After Fe atoms and Al atoms combined forming the κ phase, a region which was poor in Al atoms was formed around the κ phase. However, there was still quantities of redundant Fe left, therefore Fe atoms would form Fe-Cr phase. For the Cr atoms, the maximum solubility of Cr in copper matrix was about 0.65% (wt.). With the decrease of temperature, the solubility of Cr atoms decreased rapidly and it dropped to barely 0.05% (wt.) at 500 °C (Ref 23). Besides the formation of Fe-Cr phase could delay atomic diffusion and refined recrystallized grains which could prevent the formation of ($\alpha + \gamma_2$) eutectoid effectively and expanded the α region.

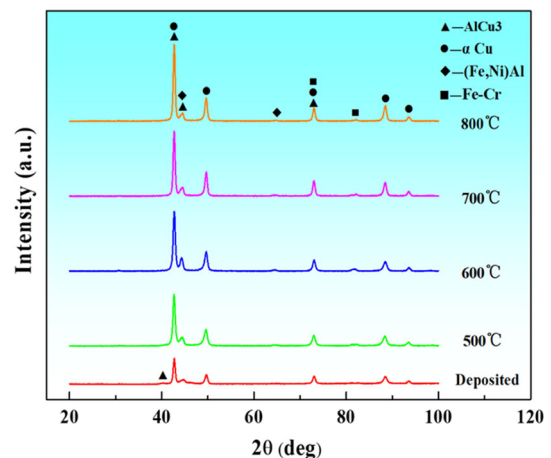


Fig. 2 XRD patterns of aluminum bronze under different heat treatment temperatures

Microstructure of laser cladding aluminum bronze coatings under different heat treatment conditions are shown in Fig. 3. The boundaries morphology between coatings and matrix under different heat treatment temperatures are shown as the Fig. 3 (a) - (e). Brighter portion is the copper rich coating and the darker portion is the iron rich substrate. A good metallurgical bonding was prepared during laser cladding process and no cracks and pores could be observed. It could be seen that after heat treatment, Fe-rich dendrites were observed to protrude from the boundary. And the Fe-Cr spherical phases could be observed. As shown in Fig. 3 (b)-(e) that the number and sizes of Fe-Cr spherical phases increased with the increase of heat treatment temperatures, and the width of Fe rich dendrites formed by element diffusion increased from 13.06 at 500 °C to 67.83 μ m at 800 °C (area within yellow dotted line). These two phenomenon cause by the increase of diffusion degree of Fe and Cr atoms into the coating during heat treatment.

Figure 3(a₁)-(e₁) show the condition of the middle part of the coatings under different heat treatment temperatures. Fe-Cr

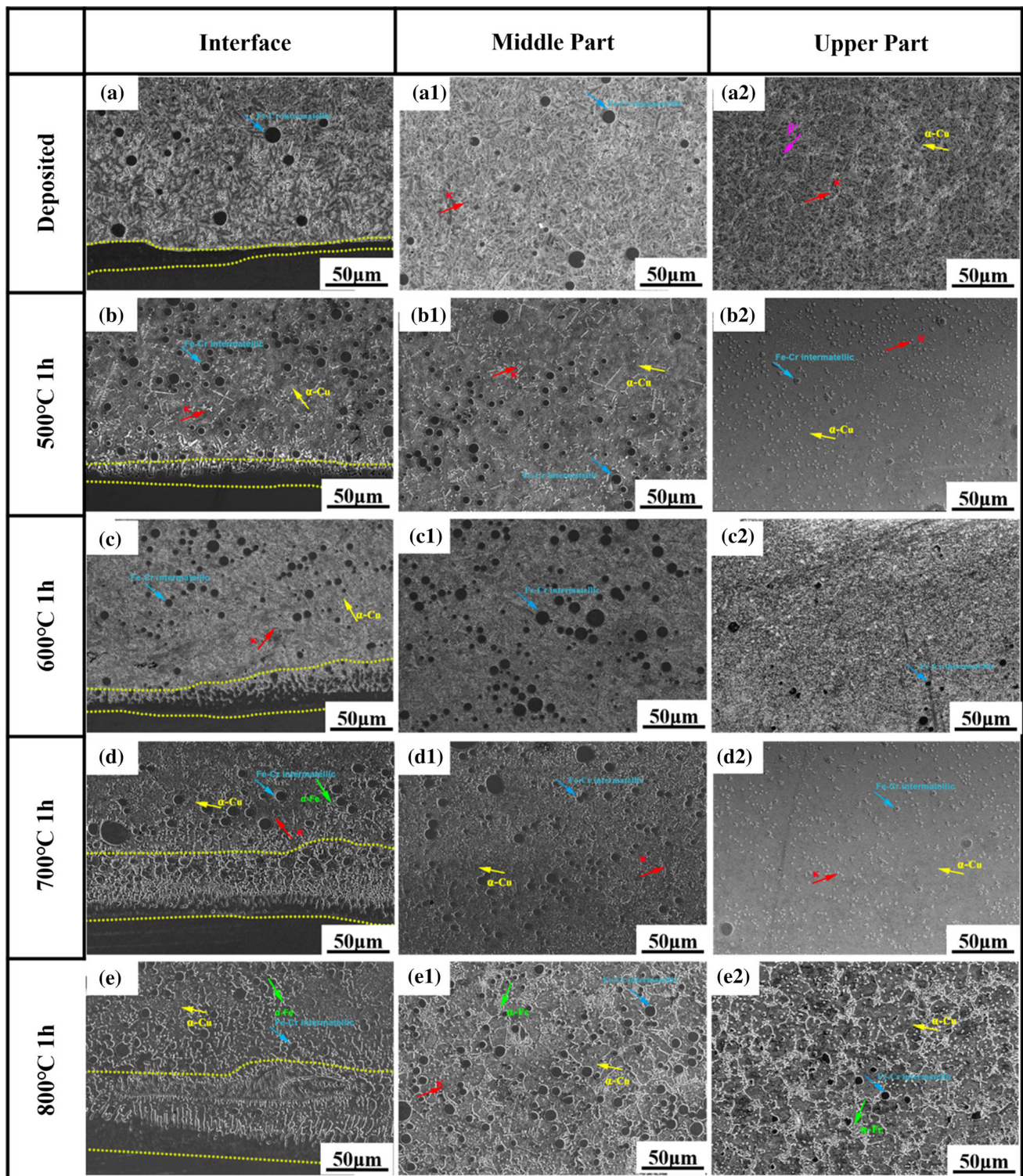


Fig. 3 SEM images of aluminum bronze under different heat treatment temperatures

rich spherical intermetallic compounds still existed in the middle of the aluminum bronze coatings under various heat treatment temperatures. However, due to the diffusion distance lengthen, the diffusion degree of Fe and Cr atoms decreased, therefore the content of Fe and Cr in the middle of the coatings was relatively lower than that at the interface.

The Fig. 3(a₂)–(e₂) show the SEM morphology of upper layer under different heat treatment temperatures. There were

differences in shapes and sizes of α -Cu, β' and κ phases on the top layer at different heat treatment temperatures. β' phase existed in deposited aluminum bronze coating caused by a non-equilibrium solidification due to a high cooling rate obtained by laser cladding. And the deposited state α -Cu consisted in the upper layer was Widmanstatten morphology which presented a fine dense needle like tissue (Ref 24). Compared to the microstructure of the α -Cu in the middle and interface of the

coatings, the microstructure in the upper part of the coatings was finer and more compact. This was because in the process of laser cladding, the post layer was tempered by the pre-deposition layer, therefore the microstructure became coarse. Deposited κ phase was also in a small size. After tempered at 500, 600, 700 and 800 °C, the eutectoid transformation was fully carried out, β' transformed into α and κ mostly, thereby β' was rarely observed in the upper part of the tempered coatings. For α and κ , as the heat treatment temperature increased, the structure coarsened significantly. Especially, α -Fe formed due to a high diffusion when the tempering temperature raised to 800 °C.

For the samples without heat treatment, the microstructure of the coatings changed greatly from the interface to the upper part of the layer. The morphology changed from the planar crystal at the interface to the sharp and dense dendrites at the middle and upper part of the layer. The temperature of liquid aluminum bronze alloy was higher than the temperature of the stainless steel matrix at the interface during the laser cladding process, and the farther away from the boundary, the higher temperature the liquid aluminum bronze alloy maintained. At this time, the temperature gradient G between liquid phase aluminum bronze alloy and 316 stainless steel solid phase was greater than 0, just given by $G > 0$. In this case, due to the high temperature of liquid aluminum bronze alloy, undercooling degree was small which led to the growth of crystal by solidified aluminum bronze alloy extended to liquid aluminum bronze interior and the growth rate was slow. Therefore, a planar crystal was formed. The temperature of the liquid aluminum bronze alloy which was a little far away from the boundary was lower, which mean the temperature gradient at this depth of layer was negative, given as $G < 0$. Due to the inner temperature of the upper part liquid phase aluminum bronze alloy was lower than the temperature of the aluminum bronze at the nearby boundary, the cooling speed was faster and cause the undercooling degree greater. Therefore, the crystal growth speed of the solidified aluminum bronze alloy grew into the liquid phase aluminum bronze alloy was extremely fast. In addition to the trunk, the dendrites also had branches as result forming typical dendrites (Ref 25, 26). The specific morphology is shown in the Fig. 3(a₁) and (a₂). Owing to the composition of elements in aluminum bronze alloy was complex, this led to the kinds and concentrations of elements in different crystal structures were different. As a result, component undercooling occurred in the coatings. Therefore, the undercooling for the formation of dendrites was reduced, and the common dendrites structure were formed in the upper and middle part of the layer.

Figure 4 demonstrates line scanning results of deposited samples and four heat treated samples. It can be seen from the line scanning curve in Fig. 4 that with the increase of the tempering temperatures, the area of mutual diffusion between matrix and coating widens, which further proved that the degree of element diffusion increases with the increase of heat treatment temperatures. It can be explained by the calculation of diffusion coefficient as follows formula (2):

$$D = D_0 \exp\left(-\frac{Q}{RT}\right) \quad (\text{Eq 2})$$

where D_0 ($\text{mol}\cdot\text{m}^{-2}\text{ s}^{-1}$) is the proportional coefficient, Q ($\text{J}\cdot\text{mol}^{-1}$) is the activation energy, R ($\text{J}\cdot\text{mol}^{-1}\text{ K}^{-1}$) is the thermodynamic constant and T (°C) is the temperature.

According to formula (1), along with the increase of T (heat treatment temperature), the diffusion coefficient of elements increase and the degree of mutual diffusion increased.

3.2 Effects of Heat Treatment on Microhardness

Figure 5 demonstrates the change of microhardness of aluminum bronze under different tempering temperature. The microhardness of interface, middle part, and upper part of deposited samples was about 222, 272 and 229 HV, respectively. Compared with the as-built coatings, after the heat treatment the microhardness improved significantly. The microhardness of the samples which tempered at 500 °C for 1 h was about 517 HV at interface and 438, 393 HV at middle and upper part respectively which was the highest one among the five samples. That was mainly because after tempered at 500 °C for 1h, a finer grain size and a amount of fine κ precipitates existed in coatings. Therefore, the combined effect of grain refinement strengthening and second phase strengthening produced a highest hardness (Ref 27).

It could be concluded from the histogram of microhardness distribution in Fig. 5 that the microhardness of the sample tempered at 600 °C for 1h is the lowest. This result was due to the inappropriate combination of size of the α -Cu phase and the intermetallic phase distribution in the sample after heat treatment as shown in Fig. 6. The microhardness of aluminum bronze coatings was mainly determined by several intermetallic phases and α -Cu phase. α -Cu is a copper rich FCC structure, which has a good ductility but low microhardness. The microhardness of Fe-Cr rich intermetallic phase and several κ phase was relatively high (Ref 14), which could significantly optimize the microhardness performance of the coatings. After tempering at 600 °C for 1 h, the heat treatment made the size of α -Cu grains increase and the microhardness of the coatings decrease significantly owing to the coarsening of α -Cu phase. Meanwhile heat treatment process provided more energy for the diffusion of metal atoms. The diffusion distance and diffusion amount of iron and chromium atoms increased. At the same time, the Fe-Cr rich phase as the second phase strengthened the coatings which improved the microhardness of the layers. But the increasing degree of microhardness was far less than the decrease of the microhardness which was caused by the grain coarsen. As a result the microhardness of the aluminum bronze coatings which tempered at 600 °C decreased obviously compared to the microhardness of the aluminum bronze coatings tempered at 500 °C. The comparison between the microhardness of the samples tempered at 700 and 800 °C for 1 h and the microhardness of tempered at 600 °C for 1 h, the former presented in a higher microhardness than the latter due to the content of the Fe-Cr rich intermetallic phase with higher microhardness in the former samples showed a higher level.

From the overall change trend of the five states, the microhardness at the surface is lower than that at the interface and it is also mentioned in previous study (Ref 28), which was mainly because the elements at the interface were more complicated than other parts. It can be seen from the microstructure in Fig. 3 that there were quantities of Fe-Cr rich spherical phase and intergranular distribution κ phase at the interface. From the microhardness distribution in Fig. 5 can also conclude that the microhardness distribution at other three tempered temperatures are much smoother than the microhardness distribution at 500 °C. This was due to the full diffusion of

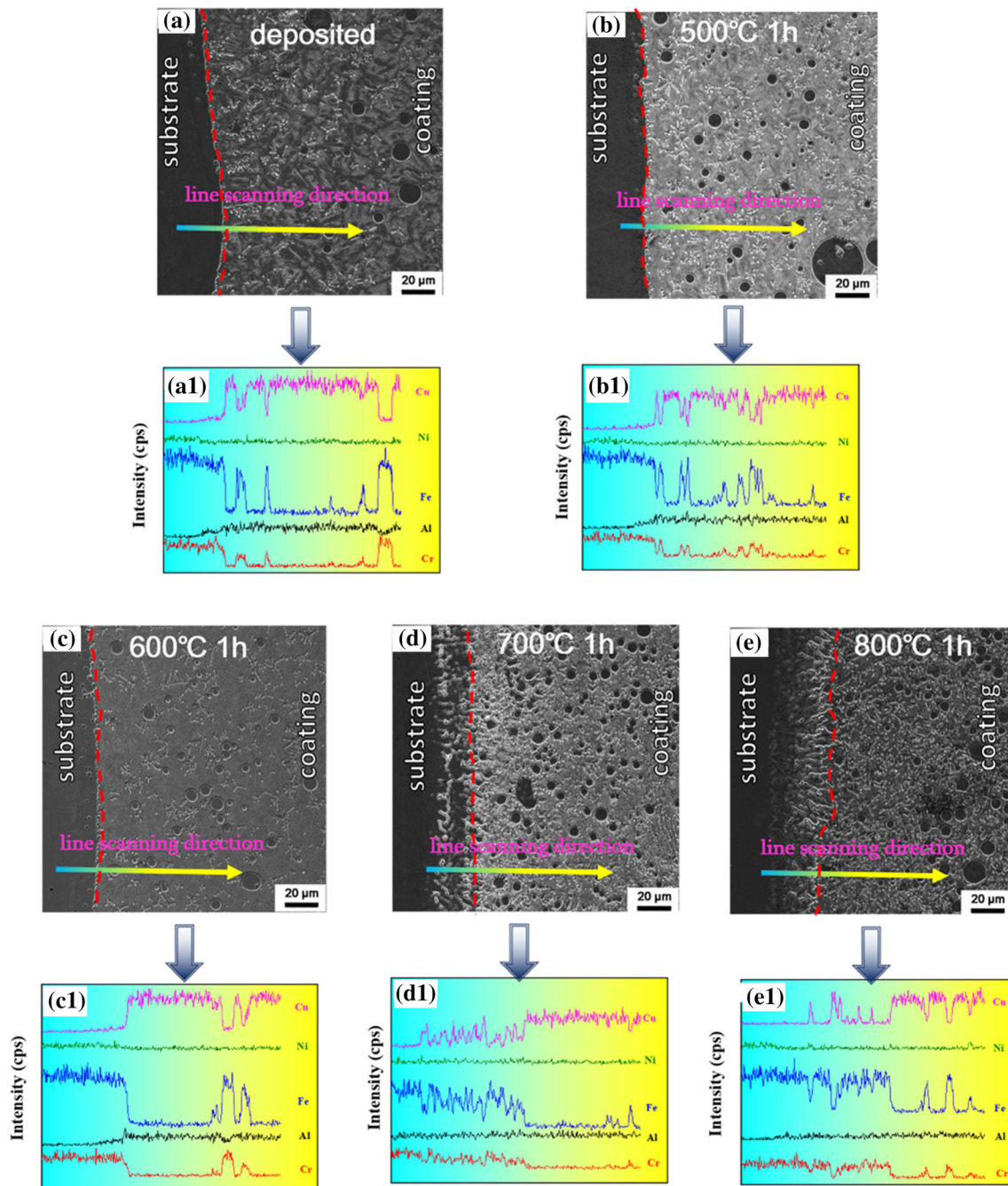


Fig. 4 Line scanning images of Cu, Fe, Al, Ni, Cr elements of aluminum bronze coatings under different heat treatment temperatures

atoms cause the microhardness of the coatings was more homogenous (Ref 4).

3.3 Effects of Heat Treatment on Wear Behaviors

The wear coefficient of the coating after tempering at different temperatures is shown in Fig. 7. Friction coefficient curves under different heat treatment conditions showed a trend of rising to a high point and then falling to a stable region. This was the result of debris accumulation in the initial stage of wear process (Ref 29). It was clear that average friction coefficient had a minimum value of 0.186 after tempering at 500 °C. And the friction coefficient increased with increase of tempering temperatures which was due to the decreased hardness

weakened the anti-bite force of the aluminum bronze coating, so as to wear resistance decreased. Different wear rate of the coatings in five different states was shown in Fig. 8. The wear rate of coatings tempered at 500 °C was lower than other samples. On the one hand, a large number of fine κ phases uniformly distributed in α matrix which hinder the slippage of the grain boundaries. On the other hand, this was related to the existence of β' phase. Aluminum bronze coatings which was in deposited state and tempered at 500 °C for 1h contained β' martensite, which would produce fine nanocrystalline structure under the worn surface caused by dynamic recrystallization induced during wear process. This part of the nanocrystalline structure effectively prevents the deformation of martensite and κ phase and reduced the wear rate (Ref 4).

SEM morphologies of the worn surface of deposited and tempered specimens after wear tests were compared and the results are shown in Fig. 9. The effect of tempering process on the microstructure of the coating changed the wear mechanism of aluminum bronze coatings. In the coatings tempered at 500 and 600 °C, abrasive wear were dominant. And the deposited and tempered at 700 and 800 °C coatings had comprehensive and complex wear mechanism of abrasive wear, adhesive wear and oxidative wear. This was mainly due to the accumulation of a large number of wear debris in the wear process. Abrasive particles generally come from the separation of Fe-Cr phase and κ phase from α phase, and the work hardened particles formed by the shear rolling of α phase. Hard particles formed grooves and wedges on the worn surface. The larger the particles, the more severe the wear. Aluminum bronze coatings tempered at 500 °C contained retained β' phase and nanoscale κ phase, which were both harder than α phase. Therefore, the deformation resistance of β' phase and κ prevented the occurrence of sever surface wear, and reducing the number of hard particles formed, and then the coatings surface showed a slight abrasive wear. Moreover, as the heat treatment temperatures increased, degree of Fe and Cr into the coatings increased, resulting in an increase in the unevenness of the coating microstructure. The increase in the unevenness of the microstructure would cause the hard phase to fall off during the wear process, and aggravate

the surface damage (Ref 30). Table 2 shows EDS results of main elements of wear debris generated during the wear process of the coatings under different conditions marked in

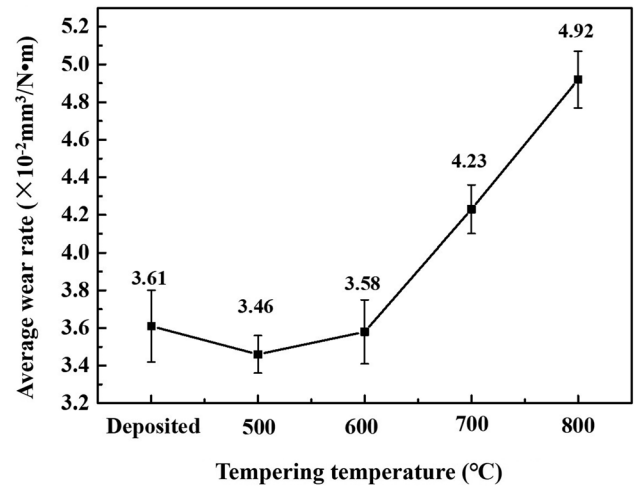


Fig. 8 Average wear rate of aluminum bronze coatings under different tempered states

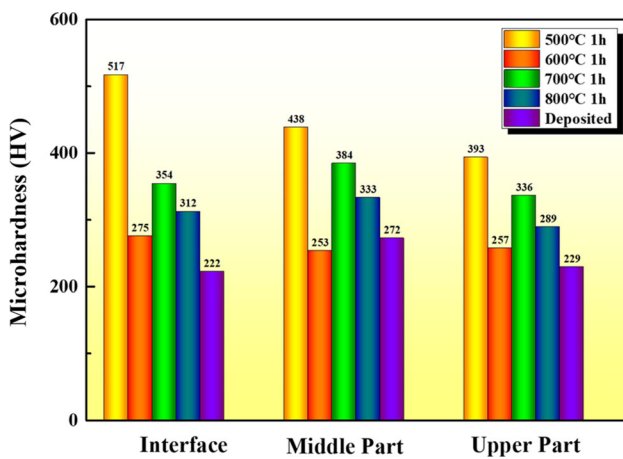


Fig. 5 The microhardness of aluminum bronze coatings and substrate with different tempered states

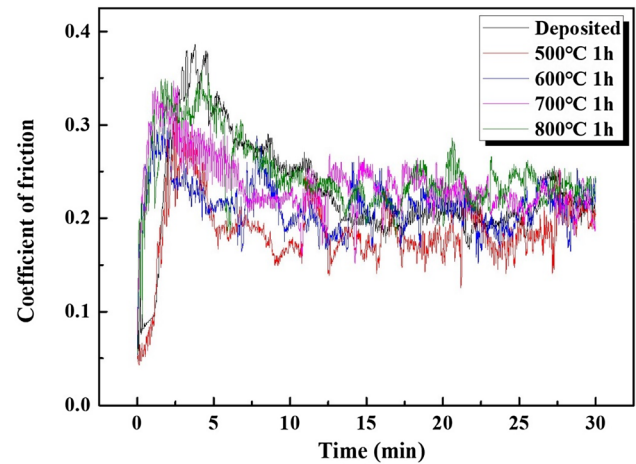


Fig. 7 Coefficient of friction during dry reciprocating sliding under different tempered states

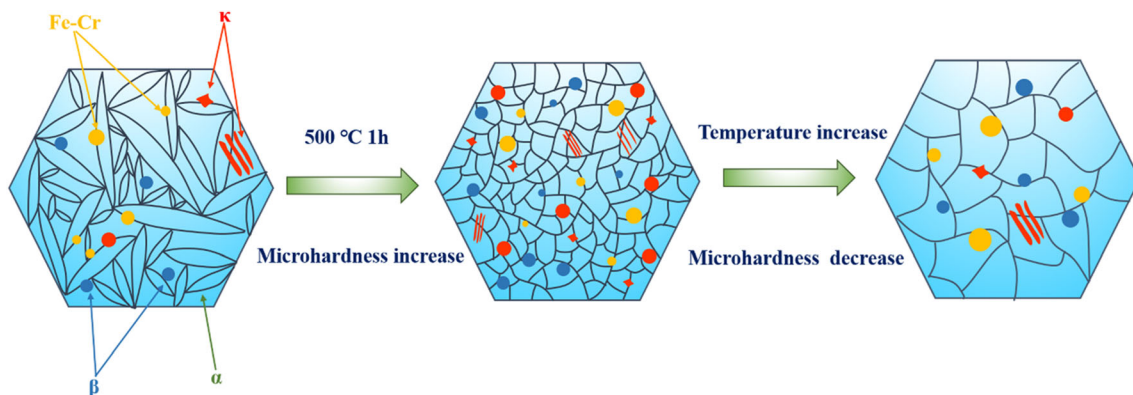


Fig. 6 Schematic diagram of microstructure evolution of aluminum bronze coatings

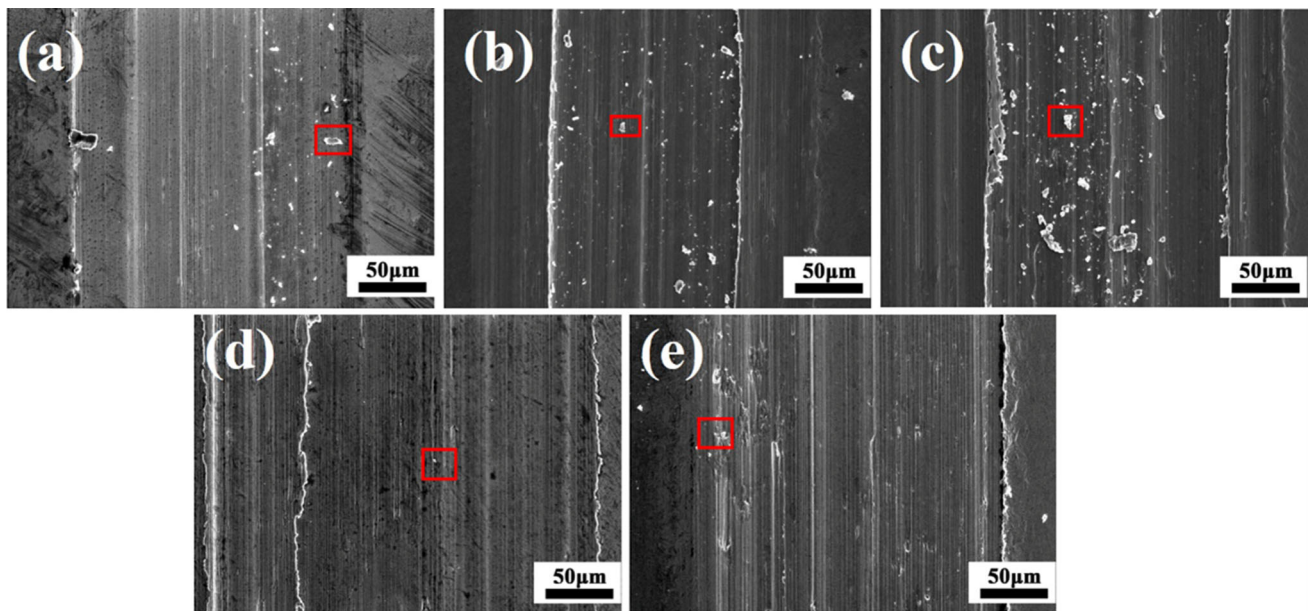


Fig. 9 Morphologies of wear surface: (a) deposited, (b) tempered 500 °C 1h, (c) tempered 600 °C 1h, (d) tempered 700 °C 1h, (e) tempered 800 °C 1h

Table 2 EDS analysis of wear debris in aluminum bronze coatings marked as Fig. 9 (all in wt.%)

	Deposited	500 °C	600 °C	700 °C	800 °C
Cu K	82.47	70.14	82.45	80.01	78.66
Fe K	6.43	5.68	4.01	6.39	6.23
Al K	11.10	11.28	11.36	10.62	10.68
O K			2.17	1.05	1.01

Fig. 9. The oxygen content in the deposited and tempered at 500 °C wear debris was low. When the heat treatment temperatures increased, the oxygen content in the film increased, which was due to the Fe content in the coating increased at high temperatures formed iron oxide (Ref 4).

3.4 EBSD Analysis

EBSD was performed to detect the change of microstructure of aluminum bronze after tempering treatment. Figure 10 shows crystallographic characterization results of the samples without heat treatment and samples tempered at 500 °C for 1 hour. The grains of the samples did not elongate along the deposition during the depositional process. This showed a same characteristic as the samples fabricated through wire-arc additive manufacturing (Ref 5). The grains of samples without heat treatment are dominated in $\langle 101 \rangle$. This is shown in the Fig. 10 that the slightly larger plates in the IPF maps seem to be mostly green. It could be due to the high temperature gradient formed by the high cooling rate during the depositional process, which led to the grain growth direction consistent with the temperature gradient direction. After tempering at 500 °C for 1 h, the grains of aluminum bronze were in random orientation and there was no preferred orientation in grain orientation. The color related to the crystallographic orientations in an individual grains was uniform. Therefore, low local stress and low

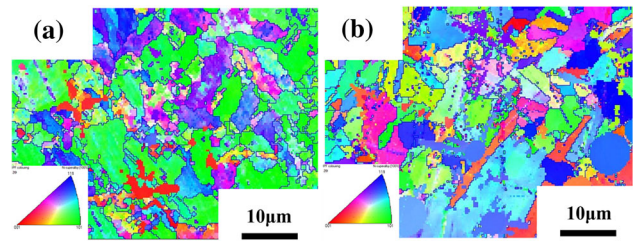


Fig. 10 EBSD maps of aluminum bronze coatings (a) deposited (b) tempered at 500 °C for 1h

dislocation density were present in aluminum bronze coatings (Ref 20, 31).

The grain misorientation angle distribution of two kind samples are shown in Fig. 11. Figure 11(a) shows the grain misorientation angle distribution of the samples without heat treatment. It can be seen that low-angle grain boundaries (LAGBs) were predominate in deposited samples. The low angle grain boundaries account for 81.8871% and the high angle grain boundaries account for 18.1129%. After tempering 500 °C for 1 h, the number of low angle grain boundaries in aluminum bronze coatings decreased and the high angle grain boundaries increased. The percentage of low angle grain boundaries decreased from 81.8871 (deposited samples) to 73.2327% (samples without heat treatment), and the percentage of high angle boundaries increased from 18.1129 (deposited sample) to 26.7673% (samples without heat treatment). Moreover, the polar distribution of grain misorientation enhancing. The high angle grain boundaries with higher energy could effectively block the slippage of dislocation which could improve the strength of the material.

The Schmidt factor distribution of the deposited samples and the samples tempered at 500 °C for 1 h was determined by EBSD. Figure 12 shows the Schmidt factor distribution of the deposited samples and heat treated samples. In the Schmidt factor distribution maps, the deeper the red, the higher the

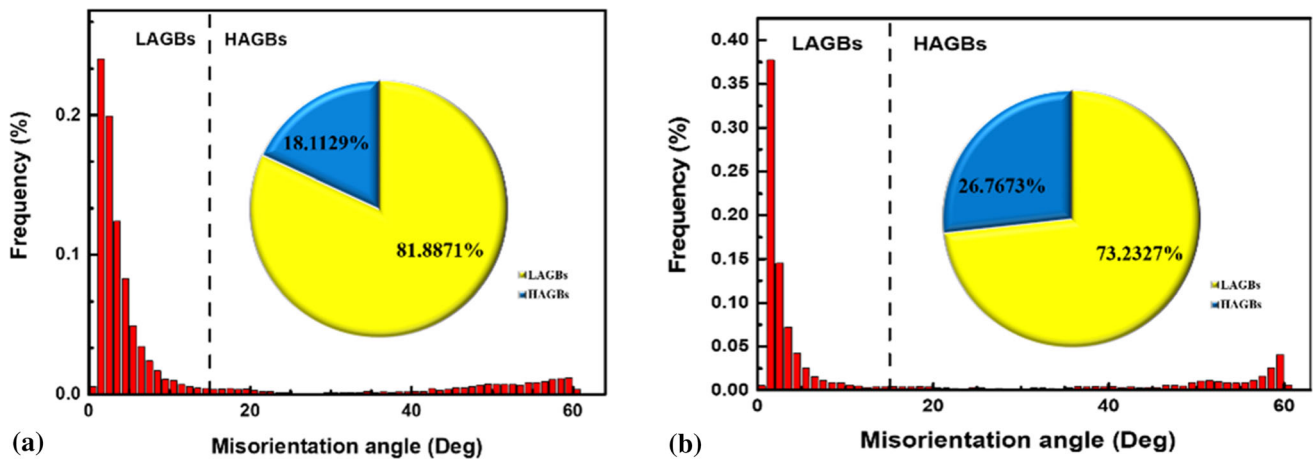


Fig. 11 Misorientation angle distribution maps of laser cladding Cu-7Al-3Fe-3Ni coatings: (a) deposited coating (b) 500 °C 1h tempered coating

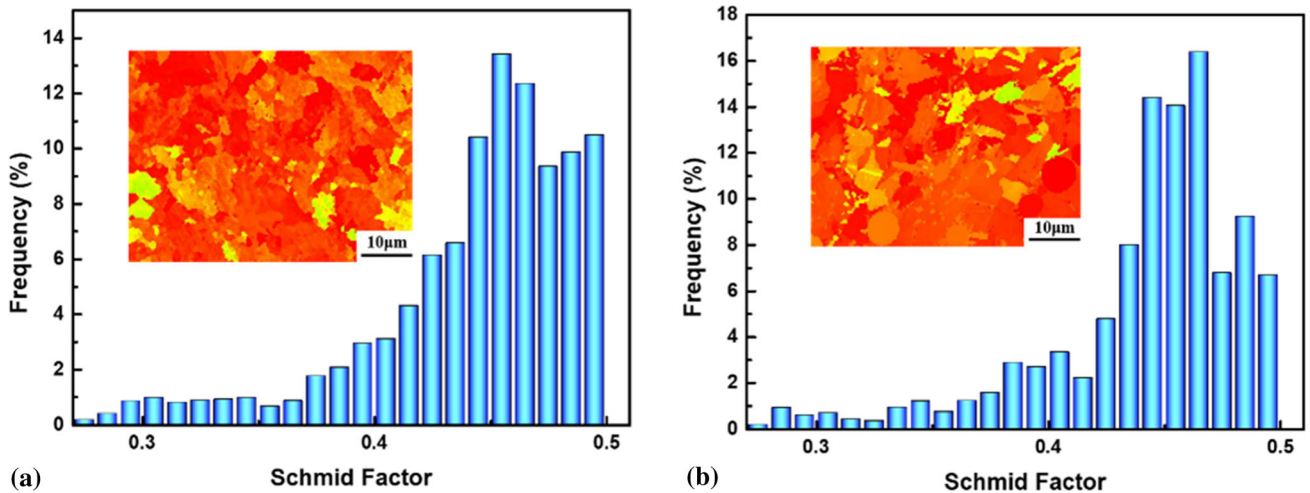


Fig. 12 The Schmid factor distribution maps of coatings before (a) and after tempering at 500 °C 1 h (b)

Schmidt factor. The Schmidt factor can illustrate the difficulty of slip (Ref 32). The higher the Schmidt factor, the easier the slip could occur. As can be seen from the figures that the Schmidt factor of the sample before heat treatment was higher than the Schmidt factor of the sample tempered at 500 °C for 1 h. Therefore, the unheated samples with higher Schmidt factor, the dislocations were easier to slip, and deformation occurred easier in unheated samples. After tempering at 500 °C for 1 h, the Schmidt factor of the samples decreased and slip were more difficult to occur, so the strength of the aluminum bronze coatings could be improved by tempering at 500 °C for 1 h.

Figure 13 shows the kernel average misorientation (KAM) distribution maps of the unheated aluminum bronze coatings and tempered samples. The misorientation of two fixed points in the crystal grain can be expressed by KAM, therefore the local plastic strain of the material can be analyzed by KAM (Ref 15). Before the heat treatment, the samples displayed a high KAM status which could be caused by the high cooling rate during the laser cladding process. After tempering, the average orientation status of the heated samples decreased but the orientation at the grain boundaries was still high.

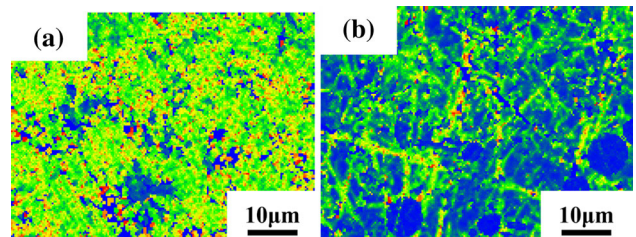


Fig. 13 KAM results of samples of aluminum bronze coatings: (a) deposited (b) tempered at 500 °C for 1 h

4. Conclusion

The aluminum bronze coating with good interface bonding was successfully prepared by laser cladding and the effects of heat treatment on aluminum bronze coatings are as follows:

- (1) The deposited aluminum bronze is mainly composed of α -Cu, β' , κ , and Fe-Cr phases. After heat treatment β' transferred into α and κ phases, and with the increase of tempering temperature, microstructure coarsened.

- (2) The changes in microstructure caused by heat treatment had a significant impact on the microhardness and wear properties of coatings. The deposited coatings and coatings tempered at 500 °C for 1h had a lower friction coefficient and wear rate due to the exist of retained β' phase and the uniform distribution of fine κ phase. When the heat treatment temperature increases, the α phase and κ phase became coarsen, the uniformity of the structure decreased, and the wear rate of the coatings increased.
- (3) After tempering at 500 °C, the texture in the deposited samples disappears. And both the LAGBs and Schmidt factor decrease, which can effectively improve the microhardness of the aluminum bronze.

Acknowledgments

The authors gratefully acknowledge to the financial support for this research from National Key Research and Development Program of China (No. 2016YFB1100204), Key Research Project from Science and Shenyang Science and Technology Funded Project (No. 19-109-1-03).

Author contributions

TY: Investigation, Writing - review & editing. SZ: Funding acquisition, Data curation. FQZ: Data curation. RJH: Data curation. CHZ: Funding acquisition, Data curation. JC: Data curation.

References

1. R.C. Barik, J.A. Wharton, R.J.K. Wood, K.S. Tan, and K.R. Stokes, Erosion and Erosion-Corrosion Performance of Cast and Thermally Sprayed Nickel-Aluminum Bronze, *Wear*, 2005, **259**, p 230–242.
2. Z. Shi, Y. Sun, A. Bloyce, and T. Belli, Unlubricated Rolling-Sliding Wear Mechanisms of Complex Aluminium Bronze Against Steel, *Wear*, 1996, **193**, p 235–241.
3. M.H. Sohi, S.M.H. Hojjatzadeh, A. Khodayar, and A. Amadeh, Liquid Phase Surface Alloying of a Nickel Aluminum Bronze Alloy with Titanium, *Surf. Coat. Technol.*, 2017, **325**, p 617–626.
4. P. Kucita, S.C. Wang, W.S. Li, R.B. Cook, and M.J. Starink, The Effects of Substrate Dilution on the Microstructure and Wear Resistance of PTA Cu-Al-Fe Aluminium Bronze Coatings, *Wear*, 2019, **440–441**, p 203102.
5. C. Dharmendra, A. Hadadzadeh, B.S. Amirkhiz, G.D. Janaki Ram, and M. Mohammadi, Microstructural Evolution and Mechanical Behavior of Nickel Aluminum Bronze Cu-9Al-4Fe-4Ni-1Mn Fabricated Through Wire-Arc Additive Manufacturing, *Addit. Manuf.*, 2019, **30**, p 100872.
6. K.S. Tan, J.A. Wharton, and R.J.K. Wood, Solid Particle Erosion-Corrosion Behaviour of a Novel HVOF Nickel Aluminium Bronze Coating for Marine Applications-Correlation Between Mass Loss and Electrochemical Measurements, *Wear*, 2005, **258**, p 629–640.
7. J.M. Chen, J. Yang, X.Q. Zhao, Y.L. An, G.L. Hou, J. Chen, and H.D. Zhou, Preparation and Properties of poly-(p)-oxybenzoyl/aluminum Bronze Composite Coating by Atmosphere Plasma Spraying, *Surf. Coat. Technol.*, 2014, **253**, p 261–267.
8. L. Wang, X.L. Xu, J.J. Xu, and Z.K. Hei, Microstructures and Properties of PVD Aluminum Bronze Coatings, *Thin Solid Films*, 2000, **376**, p 159–163.
9. E. Minni and H. Sundquist, The Structure of Aluminium Bronze Coatings Deposited by Ion Plating, *Thin Solid Films*, 1981, **80**, p 55–61.
10. C. Wang, S. Zhang, C.H. Zhang, C.L. Wu, J.B. Zhang, and A.O. Abdullah, Phase Evolution and Wear Resistance of In Situ Synthesized V8C7 Particles Reinforced Fe-Based Coating by Laser Cladding, *Opt. Laser. Technol.*, 2018, **105**, p 58–65.
11. C.L. Wu, S. Zhang, C.H. Zhang, and S.Y. Dong, Phase Evolution and Properties in Laser Surface Alloying of FeCoCrAlCuNi High-Entropy Alloy on Copper Substrate, *Surf. Coat. Technol.*, 2017, **315**, p 368–376.
12. W. Gamon and K. Anioek, Examination of the Sliding Wear of Bronze Coatings on Railway Buffer Heads, *Wear*, 2020, **448–449**, p 203235.
13. S. Nair, R. Sellamuthu, and R. Saravanan, Effect of Nickel Content on Hardness and Wear Rate of Surface Modified Cast Aluminum Bronze Alloy, *Mater. Today Proc.*, 2018, **5**, p 6617–6625.
14. X.P. Tao, S. Zhang, C.H. Zhang, C.L. Wu, J. Chen, and A.O. Abdullah, Effect of Fe and Ni Contents on Microstructure and Wear Resistance of Aluminum Bronze Coatings on 316 Stainless Steel by Laser Cladding, *Surf. Coat. Technol.*, 2018, **342**, p 76–84.
15. X. Wang, C.H. Zhang, X. Cui, S. Zhang, J. Chen, and J.B. Zhang, Microstructure and Mechanical Behavior of Additive Manufactured Cr-Ni-V Low Alloy Steel in Different Heat Treatment, *Vacuum*, 2020, **175**, p 109216.
16. C. Barr, D. McDonald, and K. Xia, Significantly Enhanced Tensile Strength and Ductility in Nickel Aluminium Bronze by Equal Channel Angular Pressing and Subsequent Heat Treatment, *J. Mater. Sci.*, 2013, **48**, p 4749–4757.
17. T. Gu, F.Q. Xu, Y.H. Zhao, and J.H. Liu, Effects of High Pressure Heat Treatment on Microstructure and Mechanical Properties of Aluminum Bronze, *Mater. Res. Express.*, 2019, **6**, p 096508.
18. X.H. Liu, D.Y. Huang, C.H. Yan, Y.J. Zhou, and W.L. Yan, Multi-Directional Forging and Aging Treatment Effects on Friction and Wear Characterization of Aluminium-Bronze Alloy, *Mater. Charact.*, 2020, **167**, p 110511.
19. T. Murray, S. Thomas, Y.X. Wu, W. Neil, and C. Hutchinson, Selective Laser Melting of Nickel Aluminum Bronze, *Addit. Manuf.*, 2020, **33**, p 101122.
20. C. Dharmendra, B.S. Amirkhiz, A. Lloyd, G.D. Janaki Ram, and M. Mohammadi, Wire-Arc Additive Manufactured Nickel Aluminum Bronze with Enhanced Mechanical Properties Using Heat Treatments Cycles, *Addit. Manuf.*, 2020, **36**, p 101510.
21. X. Wang, C.H. Zhang, X. Cui, S. Zhang, J. Chen, and J.B. Zhang, Novel Gradient Alloy Steel with Quasi-Continuous Ratios Fabricated by SLM: Material Microstructure and Wear Mechanism, *Mater. Charact.*, 2021, **174**, p 111020.
22. E.A. Culpán and G. Rose, Microstructural Characterization of Cast Nickel Aluminium Bronze, *J. Mater. Sci.*, 1978, **13**, p 1647–1657.
23. S. Cui and I.H. Jung, Thermodynamic Modeling of the Cu-Fe-Cr and Cu-Fe-Mn Systems, *Calphad*, 2017, **56**, p 241–259.
24. D.M. Lloyd, G.W. Lorimer, and N. Ridley, Characterization of Phases in a Nickel-Aluminium Bronze, *Met. Technol.*, 1980, **7**, p 114–119.
25. M. Zhang, G.L. Zhao, X.H. Wang, S.S. Liu, and W.L. Ying, Microstructure Evolution and Properties of In-Situ Ceramic Particles Reinforced Fe-Based Composite Coating Produced by Ultrasonic Vibration Assisted Laser Cladding Processing, *Surf. Coat. Technol.*, 2020, **403**, p 126445.
26. J.W. Chen, C.H. Zhang, F.Q. Zhou, Z. Song, H.T. Chen, and Q. Wang, Microstructural, electrochemical and wear-corrosion characterization of TC4-5Cu alloy fabricated by selective laser melting, *J. Alloys Compd.*, 2021, **874**, p 159953.
27. M.R. Rahul and G. Phanikumar, Growth Kinetics, Microhardness and Microstructure Evolution of Undercooled FeCoNiCuSn High Entropy Alloy, *Mater. Sci. Eng. A.*, 2020, **777**, p 139022.
28. Y.T. Lv, B. Nie, L.Q. Wang, H.Z. Cui, L. Li, R. Wang, and F.Y. Lyu, Optimal Microstructures on Fatigue Properties of Friction Stir

- Processed NiAl Bronze Alloy and Its Resistant Fatigue Crack Growth Mechanism, *Mater. Sci. Eng. A*, 2020, **771**, p 138577.
29. L.J. da Silva and A.S.C.M. D'Oliveira, NiCrSiBC Coatings: Effect of Dilution on Microstructure and High Temperature Tribological Behavior, *Wear*, 2016, **350–351**, p 130–140.
 30. W.S. Li, Z.P. Wang, Y. Lu, Y.H. Yuan, and F. Wang, Mechanical and Tribological Properties of a Novel Aluminum Bronze Material for Drawing Dies, *Wear*, 2006, **261**, p 155–163.
 31. Y. Zhang and Y. Yin, Investigation into the Manufacturing Process and Properties of BrAl10Fe4 Aluminium-Bronze Parts by Selective Laser Melting, *Mater. Technol.*, 2020, **2**, p 1–15.
 32. W.J. Zhang, J.X. Lu, J. Wang, L.J. Sang, J.Y. Ma, Y.F. Zhang, and Z. Zhang, In-Situ EBSD Study of Deformation Behavior of Inconel 740H Alloy at High-Temperature Tensile Loading, *J. Alloys Compd.*, 2020, **820**, p 153424

Publisher's Note Springer Nature remains neutral with regard to jurisdictional claims in published maps and institutional affiliations.